Electronic Supplementary Information

Faradaic Processes beyond Nernst's Law: Density Functional Theory Assisted Modelling of Partial Electron Delocalisation and Pseudocapacitance in Graphene Oxides

Junfu Li,[a] James O'Shea,[b] Xianghui Hou,[a] and George Z. Chen*[a c]

[a] Advanced Materials Research Group, Faculty of Engineering, University of Nottingham, Nottingham NG7 2RD, UK

[b] School of Physics and Astronomy, University of Nottingham, Nottingham NG7 2RD, UK

[c] Energy Engineering Research Group, Faculty of Science and Engineering, University of Nottingham Ningbo China, Ningbo 315100, P. R. China

*** E-mail: george.chen@nottingham.ac.uk**

S1. Methodology

Only epoxy groups are considered as functionalities to segment the ED areas in GO models. By simply tuning their coverage on the basal plane of GOs, both the degrees of oxidation and ED can be modified and controlled. Only the Type-II fully oxidised graphene (FOG) structure is considered, since it has been theoretically proven to be the most stable configuration.[1] Electron delocalisation areas (EDAs) are defined as the columns of π-conjugated double-bond carbon chains extending along the [010] direction of the unit cell of GOs. These EDAs are separated by a certain width of epoxy group covered areas. Details of established models are collected in **Fig. S1** (a1-n1) in which computational methodologies, parameter settings and criteria of calculation accuracy are also described.

S2. Modelling

The atomic structure of graphene oxides (GO) has been studied for over 80 years, since Hoffmann *et al*., proposed a structure in which the O atoms in graphite oxide are bound to the C atoms in the basal plane.[2, 3] From this early work, there was evidence that hydroxyl groups are also present in graphite oxide.[3, 4] Solid state ^{13}C NMR studies provided evidence for C–OH, C–O–C, and >C=C< groups in graphite oxide[5] and[6]. In summary, The GOs consist of a one-atom thick layer of graphene randomly decorated with oxygen-containing functional groups such as carbonyl(>C=O), hydroxyl (⩾C-OH or >C-OH), epoxy(⩾C-O-C⩽ or >C-O-C<), and ether groups(>C-O-R' or ⩾C-O-R').[7] Here, '⩾C-' symbol, differed from '>C-', is used to represent those in-plane carbon atoms of GO with *sp*^{3} hybridisation by bonding with another heteroatom, and '>C-' the edge carbon atoms. It is evident that carbonyl and ether groups normally arise on the edge of the GO layer as well as that of hole defects. Based on previous studies,[8-12] the epoxy group (⩾C-O-C⩽) is identified as the most dominant species compared with the other three functionalities: bonding hydrogen (⩾C-H), hydroxyl (⩾C-OH) and peroxide (⩾C-O-O-C⩽),[8] which mainly resided on the basal plane of graphite and graphene rather than on edge. Moreover atomic force microscopy (AFM) measurements showed that the GO sheets appear to have a thickness equal to integer multiples of ~6.7 Å,[9]

indicating that epoxy groups are likely to exist on both sides of the graphene layer.[13] So, in this study, epoxy groups were considered to build the target models of GO. This kind of periodic structure with parallel strips of epoxide and clean graphene ribbons has been proved to be more energetically favourable, namely a comparable stability.[14] All graphene and graphene oxide structures were located in the x-y (a-b) plane and modelled in a hexagonal or rectangular supercell with periodic boundary conditions. In order to eliminate interactions between neighbouring GO sheets and thus to simulate a single layer of GO, the z (c) -axis constant was set to 20 Å between each GO layer in a unit cell. Detailed geometry configurations are shown in below **Fig. S1** (a1-n1).

S3. Computational method

The First-principles density functional theory (DFT) calculations were performed using the academic CASTEP package version 7.0.3 and using Materials Studio 5.0 (Accelrys) as the interface and visualizer. The CASTEP is a quantum mechanics-based program, which employs the density functional theory and plane-wave pseudopotential method.[15] The electronic exchange and correlation effects were described within the generalized gradient approximation (GGA) using the Perdew Burke Ernherzhof (PBE) functional,[16] which has been widely used in theoretical predictions of the electronic structure for graphene and its derivatives.[11,17-19] All calculations were carried out on the models shown in **Fig. S1** under the same ultra-fine energy cut-off (380 eV) for the plane wave basis set. This cut-off energy was ascertained by a forehand convergence testing. A desktop computer with a single Intel Core i3-4130 CPU @ 3.40GHz, 8.0 GB RAM memory and 1 T hard disk drive was used for all calculations. The Brillouin zone sampling was performed with three to four special Monkhorst–Pack k-points[20] as shown in beneath **Fig. S2**. Three k-points of Γ-K-M were assigned to pure graphene, four k-points of Γ-K-M-B for GOs depending on the shape of the reciprocal lattice and Brillouin zone. The k-points sampling in this work followed a principle of computer resource saving without sacrificing the calculation accuracy. That is to say by using the minimum numbers of sampling in the Brillouin zone to achieve a proper Brillouin zone integration without lose too much accuracy with the energy band calculation. In fact, pre-calculation had been carried out by gradually increase the number of k-points for all as-defined GO species shown in Fig. S1. Results indicated that no apparent variation can be observed under a finer sampling, namely more k-points, especially for the fully oxidised graphene (FOG) because of its relatively wide energy gap. But this is not the case for POG species, theoretically, higher sampling density in the Brillouin zone means a higher resolution for the energy states and DOS, which is very critical for inspecting species with narrow energy gap and/or fine extra energy states fairly close to the Fermi level. Of course denser sampling in the Brillouin zone again means higher demanding of computational resource. Therefore based on our pre-calculation results, the k-points sampling were ascertained and shown in the last volume of Table. S1. Only spin-paired calculations were performed in this study since tests demonstrated negligible effects of spin-polarization. The geometry optimisations were carried out with Broyden–Fletcher–Goldfarb–Shanno (BFGS) algorithm[21] and its quality was set to perform the calculation until the energy tolerance was below 2.0×10^{-5} eV/atom, atomic forces were below 0.05eV/Å, maximum stress tolerance was below 0.1 GPa,

and maximum displacement tolerance was below 0.002Å. The self-consistent field (SCF) tolerance and k-point set of electronic structure calculations, including energy band and density of states, were set to a convergence threshold of 5×10^{-7} eV/atom (Ultra-Fine). The electronic structures of the above models were calculated in the first Brillouin zone (the grey zone encircled by a dashed line) of each crystal structure following the path as shown in **Fig. S2** (a-c). A smearing integration method with a smearing width of 0.2 eV was used to obtain the DOS diagram. Because this value is approximately equal to the thermodynamic fluctuation at room temperature.

In order to investigate the influence of different sizes and separations of EDAs, chains of epoxy groups were removed from GO leaving various degrees of π-conjugated zones. These zones varied in width from one zigzag carbon chain to three, and the distance between each zone was controlled by the coverage of epoxy groups ranging from one to four columns. These structures can not only represent partially reduced or oxidised graphene oxides, but also have distinguishable degrees of electron delocalisation. The electronic structures of the above optimised models were calculated in the first Brillouin zone in **Fig. S2** (a-c).

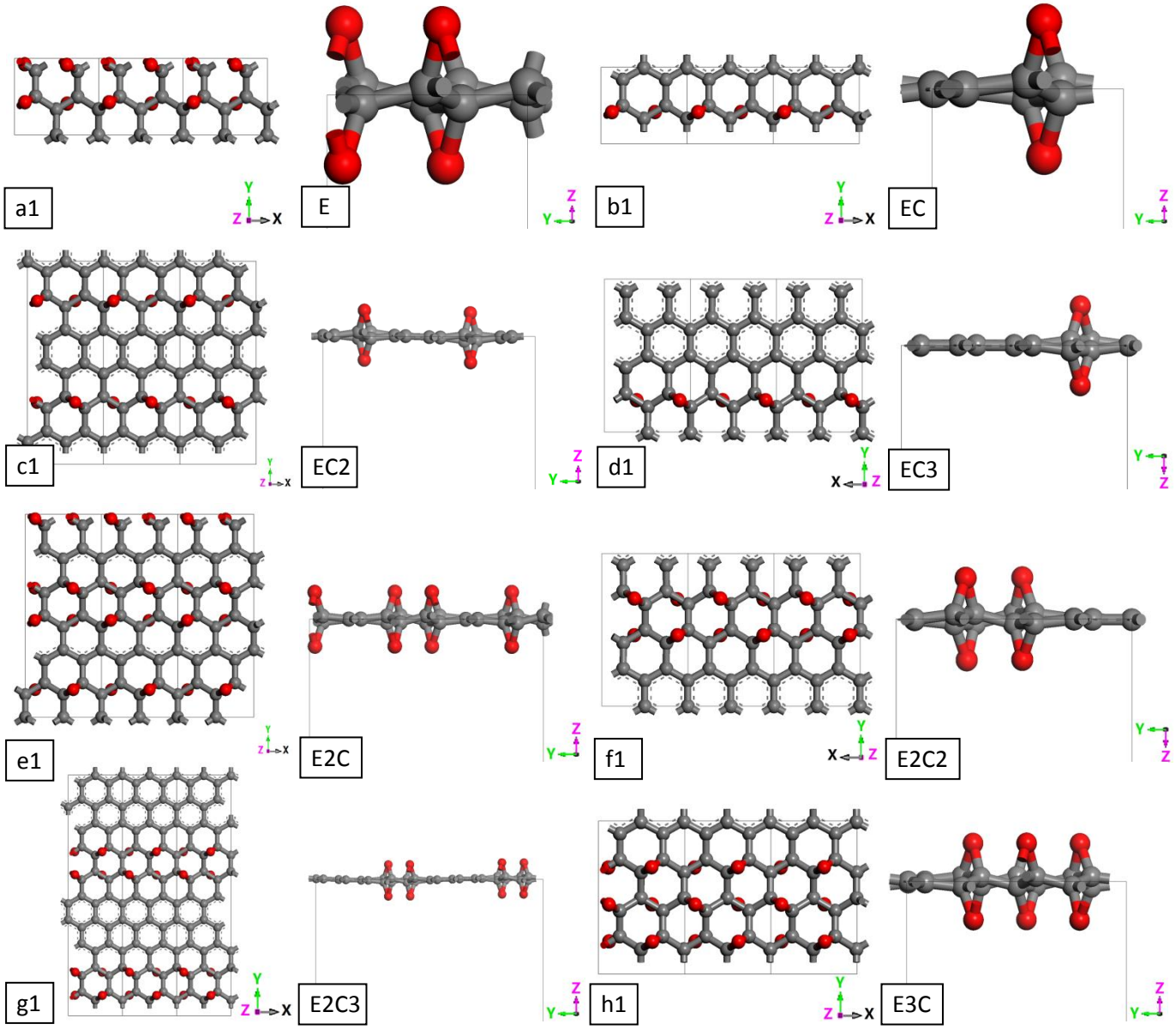

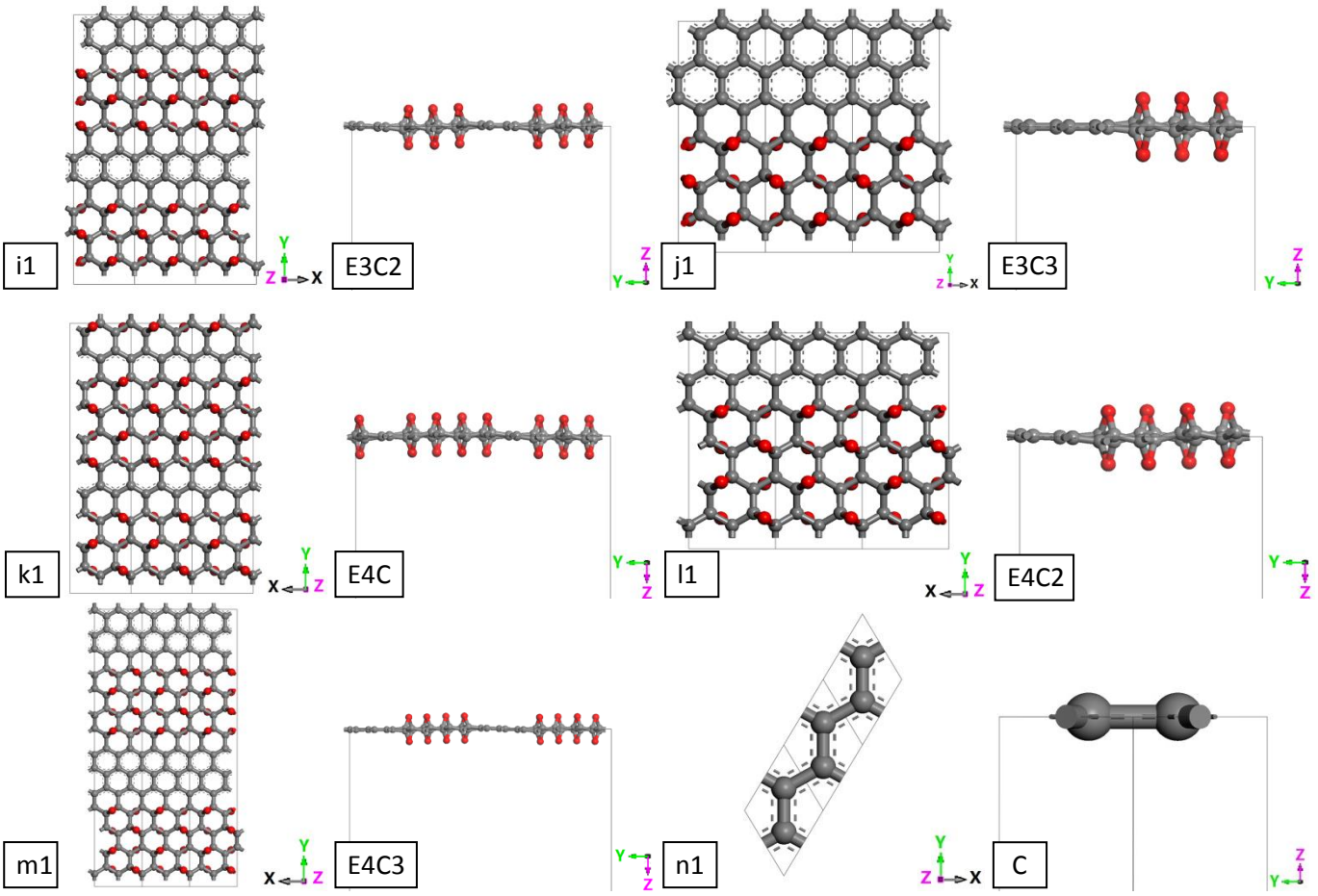

Fig. S1 Fully optimised geometry structures of fully GO (a1), partially redox GO (b1-m1), graphene (n1), and corresponding side views of each unit cell labelled in abbreviated forms as used in Table 1 and Table S1.

As shown by the results in **Fig. S3** (c-n), all the partially reduced or oxidised GO models have a very similar electronic band structure, especially around the Fermi level. In fact, the two closest energy levels, above and below the E_F, are derived from p_z orbital of carbon atoms and the *2p* orbitals of oxygen atoms. Differing from the Dirac distribution at the K point of PG, a part of flat energy bands close the E_F, along Γ to K in POGs, extends wider in E-k space as EDAs increase. Significantly these flat bands resulting in a higher electronic density of states (DOS) can enhance the electron confinement effect and the quantum capacitance00. which is directly correlated to the DOS,[22, 23] therefore can benefit the storage of electrons/holes within these delocalised states in some range of energy level, in other words, improving the ability of charge storage within these delocalised region. In the first sequence of models (**Fig. S3** c, d and e), only one column of epoxy group separates two neighbouring EDAs which varied from one to three columns of zigzag carbon double-bonds. It was found that the energy gap (E_g) changed non-linearly from 0.496 eV, sharply decreased to 0.041 eV, and then increased to 0.289 eV. Since the thermal equilibrium fluctuation at 298 K is on the order of 0.1 eV, the second model in this sequence is almost a conductor for this thermal fluctuation owing to its narrow E_g. The second sequence of models, in **Fig. S3** f, g and h, had two

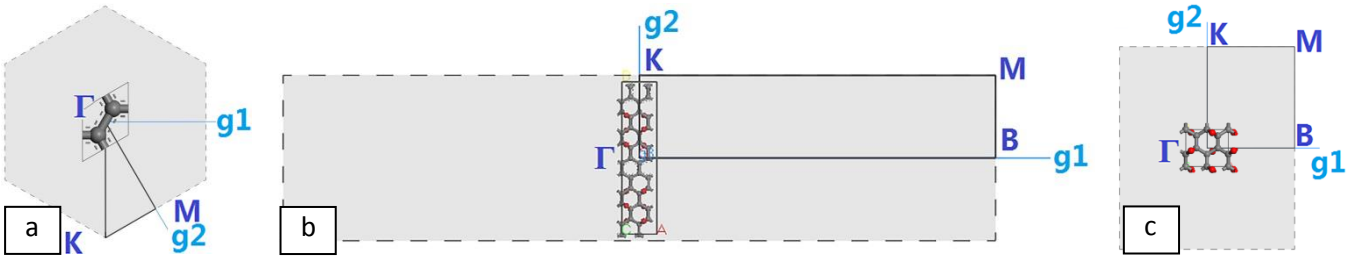

Fig. S2 Brillouin zones of (a) pure graphene unit cell, (b) partially oxidised and (c) fully oxidised graphenes.

columns of epoxy groups separating the neighbouring zones of ED which again increased from one to three zigzag chains of carbon double-bonds. E_g narrows down from 0.429 eV (semi-conductivity) to 0.182 eV, and then vanishes to 0.0 eV (full conductivity). In the following third (**Fig. S3** i, j and k) and fourth (**Fig. S3** l, m and n) sequences of models, E_g decreases in a similar trend from 0.666 eV to 0.145 eV, then to 0.027 eV and from 0.513 eV to 0.227 eV, then to 0.011 eV respectively. Again, the last structures in these two sequences were almost conductors. The origin of these narrow E_gs have been ascribed to both the breakdown of sub-lattice symmetry in graphene by the epoxy groups and the change in carbon hybridization from sp^2 to sp^3 due to strong covalent bonding between C and O[13]. In addition, we propose that the EDAs also play a role in determination of these discretely narrow E_gs by interference with the epoxy group bonding areas. In terms of the DOS, all models, except FOG and PG, show very similar distributions. Peaks between −20 and −25 eV correspond mainly to the 2s orbital of O from the epoxy groups. Comparing absolute DOS intensities between unit cells is of limited value because the actual intensity of DOS is proportionated to the numbers of atoms within the unit cell. However, the intensity of DOS around Fermi level, which can be considered as extra states originating from the p-orbitals of the carbon atoms, increases with increasing EDA (see through the same column of **Fig. S3**, e.g. c to e or f to h), but decreases slightly with the extension of the epoxy group coverage (see through the same row of **Fig. S3**, e.g. c to l or d to m).

S4. Projected DOS (PDOS) analyses

PDOS analyses were carried out on two representative POGs showing apparent extra energy states near the Fermi level, e.g. the species of E2C3 and E3C2. Carbon atoms in GOs can be classified into two groups. The one in which carbon atoms are completely bonded with its four sp^3 orbitals with the neighbouring carbon atoms or oxygen atoms; the other one in which carbons maintained the π-conjugated double bonds. As shown in **Fig. S4**, It is indicated that carbon atoms within the sp^2 region, namely the electron delocalisation region, contribute a main portion to the PDOS population densities of as-observed extra energy states near the Fermi level, especially from the p-orbital of these double bond carbon atoms. For fully-localised carbon and oxygen atoms, they only contribute a negligible parts in the PDOS. Therefore, it is rational to assign those extra bands to the delocalised electrons on the carbon atoms within the π-conjugated region rather than those carbon atoms sp^3-bonded with

oxygen atoms. And the author believe that it is these discrete extra energy bands play a key part in the charge storage mechanism of pseudocapacitance as long as they hold a proper distribution within the operating potential window of electrode materials. This type of charge storage is apparently in a faradic way, but distinguishes from a faradic process arising from a redox process. Because the later definitely follows the Nernstian law with a peak-like current response, however the pseudocapacitance should be a capacitive faradic process appearing a rectangular CV response. Therefore this EDLC-like capacitive behaviour, namely pseudocapacitance, may be attributed to the special electronic structure studied in the present paper.

Table S1. Detailed structure parameters of each GOs models and pure graphene after geometry optimisation

Models	**Molecular Formula** [a]	**Unit Cell Parameters**	**Abbreviated forms** [b]	**Number of k-points used in calculation**[c]
FOG	C_2O	SpaceGroup: P1 α = 90°, β = 90°, γ= 90° A = 4.27 Å, B = 4.93 Å, C = 20 Å C-C bond length: 1.43-1.46 Å C=C bond length: N/A C-O bond length: 1.45 Å	E	3×3×1
Partially reduced GO (POG)	C_4O	SpaceGroup: P1 α = 90°, β = 90°, γ= 90° A = 4.93 Å, B = 4.27 Å, C = 20 Å C-C bond length: 1.45-1.46 Å C=C bond length: 1.37-1.42 Å C-O bond length: 1.465 Å	EC	5×7×1
	C_6O	SpaceGroup: P1 α = 90°, β = 90°, γ= 90° A = 4.93 Å, B = 12.81 Å, C = 20 Å C-C bond length: 1.45-1.46 Å C=C bond length: 1.40-1.42 Å C-O bond length: 1.47 Å	EC2	5×5×1
	C_8O	SpaceGroup: P1 α = 90°, β = 90°, γ= 90° A = 4.93 Å, B = 8.54 Å, C = 20 Å C-C bond length: 1.45-1.47 Å C=C bond length: 1.40-1.42 Å C-O bond length: 1.46 Å	EC3	5×3×1
	C_3O	SpaceGroup: P1 α = 90°, β = 90°, γ= 90° A = 4.93 Å, B = 12.81 Å, C = 20 Å C-C bond length: 1.44-1.46 Å C=C bond length: 1.37-1.42 Å C-O bond length: 1.44-1.48 Å	E2C	5×2×1
	C_4O	SpaceGroup: P1 α = 90°, β = 90°, γ= 90° A = 4.93 Å, B = 8.54 Å, C = 20 Å C-C bond length: 1.45-1.47 Å C=C bond length: 1.40-1.42 Å C-O bond length: 1.44-1.48 Å	E2C2	5×3×1

	C_5O	SpaceGroup: P1 α = 90°, β = 90°, γ= 90° A = 4.93 Å, B = 21.35 Å, C = 20 Å C-C bond length: 1.45-1.47 Å C=C bond length: 1.40-1.42 Å C-O bond length: 1.44-1.48 Å	E2C3	5×1×1
	C_8O_3	SpaceGroup: P1 α = 90°, β = 90°, γ= 90° A = 4.93 Å, B = 8.54 Å, C = 20 Å C-C bond length: 1.45-1.47 Å C=C bond length: 1.36-1.42 Å C-O bond length: 1.44-1.46 Å	E3C	5×3×1
	$C_{10}O_3$	SpaceGroup: P1 α = 90°, β = 90°, γ= 90° A = 4.93 Å, B = 21.35 Å, C = 20 Å C-C bond length: 1.44-1.47 Å C=C bond length: 1.40-1.42 Å C-O bond length: 1.44-1.48 Å	E3C2	5×3×1
	C_4O	SpaceGroup: P1 α = 90°, β = 90°, γ= 90° A = 4.93 Å, B = 12.81 Å, C = 20 Å C-C bond length: 1.44-1.47 Å C=C bond length: 1.40-1.42 Å C-O bond length: 1.44-1.48 Å	E3C3	5×3×1
	C_5O_2	SpaceGroup: P1 α = 90°, β = 90°, γ= 90° A = 4.93 Å, B = 21.35 Å, C = 20 Å C-C bond length: 1.43-1.46 Å C=C bond length: 1.36-1.42 Å C-O bond length: 1.44-1.47 Å	E4C	5×1×1
	C_3O	SpaceGroup: P1 α = 90°, β = 90°, γ= 90° A = 4.93 Å, B = 12.81 Å, C = 20 Å C-C bond length: 1.44-1.46 Å C=C bond length: 1.40-1.42 Å C-O bond length: 1.44-1.48 Å	E4C2	5×3×1
	C_7O_2	SpaceGroup: P1 α = 90°, β = 90°, γ= 90° A = 4.93 Å, B = 29.90 Å, C = 20 Å C-C bond length: 1.44-1.47 Å C=C bond length: 1.40-1.42 Å C-O bond length: 1.44-1.48 Å	E4C3	5×1×1
PG	C	SpaceGroup: 6/mmm α = 90°, β = 90°, γ= 120° A = 2.47 Å, B = 2.47 Å, C = 20 Å C-C bond length: N/A C=C bond length: 1.42 Å C-O bond length: N/A	C	20×20×1

[a] This is the nominal molecular fomula also indicates the ratio of carbon to oxygen atoms ;

[b] E represents the column number of epoxy groups, C the π-conjugation column number;

[c] The corresponding direction in the reciprocal space is a×b×c, and c is perpendicular to the basal plane of graphene00.

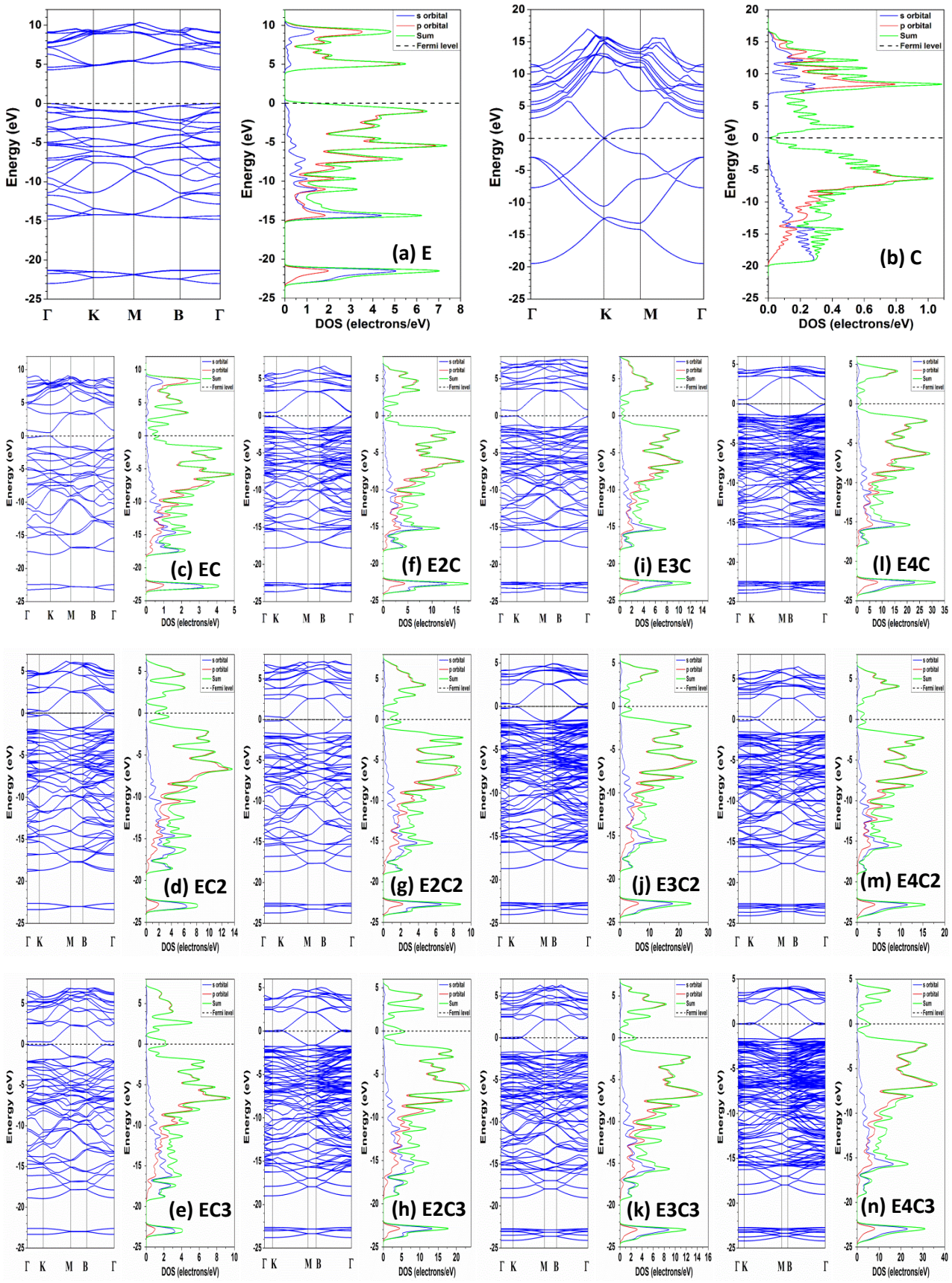

Fig. S3 All calculation results of the energy band structures and density of states: (a) fully oxidised graphene, (b) pure graphene and (c-n) partially oxidised graphene.

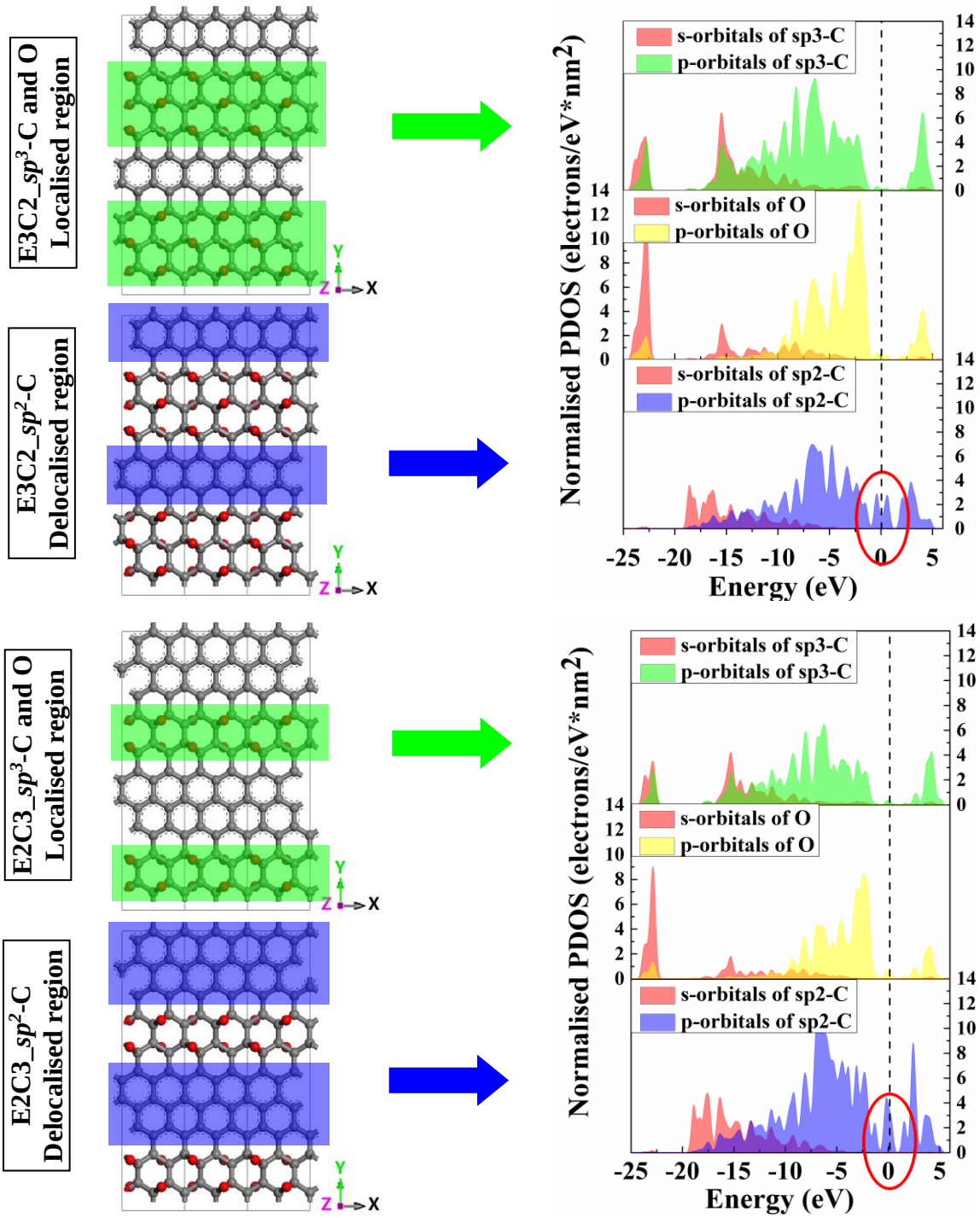

Fig. S4 Projected DOS analyses on two representative POG species, E3C2 and E2C3. The carbon atoms enclosed in blue rectangular are so-called electron delocalised region; in green rectangular are electron localised region.

S5. Voltammetric behaviour of different electrode processes

In the following discussion, the electrochemical convention is followed, i.e., the electrolyte is a liquid and ionic conductor but an electronic insulator, and the electrode material is an electronic conductor or semiconductor. When in contact with an electrolyte under a linear and cyclic scanning potential, i.e. the

conditions for cyclic voltammetry, an electrode may respond in differently ways, producing various cyclic voltammograms (CVs) whose shapes can be an indicator of the nature of the electrode process. These are briefly discussed below with reference to the redox activities of the electrode material and the electrolyte.

S5.1. First of all, it is worth mentioning that in classic terms of electrochemistry, the current recorded in cyclic voltammetry can originate from either or both of chemical and physical changes on the electrode. The physical change induced current is the charging and discharging of the so called electric double layer (EDL) at the interface between the electrode and electrolyte. In such cases, ions are electro-adsorbed on the electrolyte side of the electrode|electrolyte (E|E) interface, whilst electrons or holes accumulate on the electrode side. Note that in such physical charging/discharging processes, no electron transfer occurs crossing the E|E interface, but the ionic and electronic charges remain separated on each side of the interface. Here, the E|E interface, which is an exchangeable term of EDL, behaves like a capacitor for charge storage and release. Consequently, the charging/discharging currents are termed as being electrochemically capacitive or simply capacitive. Capacitive behaviour is typically featured by a rectangular cyclic voltammogram (CV) as shown in **Fig. S5**a.

Experimentally, a capacitive CV can be observed on an electrode made from an electrochemically and chemically inert but electronically conductive porous material, e.g. graphite or activated carbon, in a redox inactive electrolyte. It should be pointed that for any known material, the potential range in which the capacitive CV is recorded is known as the capacitive potential range (CPR) and it is in fact a key electrochemical parameter for materials characterisation. Beyond the either side of the CPR, either the electrode material or the electrolyte or both will undergo decomposition reactions.

S5.2. When chemical processes involve electron transfer crossing the interface between two different phases, including but not limited to the E|E interface and that between an electrode substrate (i.e. current collector) and a redox active coating, they are termed as Faradic processes.

In the electrochemical cell mentioned in (1), addition of a reducible species, O, into the liquid electrolyte will lead to a couple of asymmetrical current peaks on the CV as shown in **Fig. S5**b, if the reduction of O to form the reduced species, R, i.e. $O + ne \rightleftharpoons R$, is electrochemically reversible. This behaviour can be predicted by Nernst's Law under control of diffusion of O or R in the electrolyte governed by Fick's Laws. Particularly, the activities of O and R in the electrolyte near the electrode surface can be described by the Nernst Equation, i.e. $E = E^o + (RT/n\mathrm{F})\ln(a_O/a_R)$ where E is the applied or measured electrode potential, E^o the standard potential of the redox couple of O and R, n the number of electrons transferred between O and R, and a_O and a_R the activities of O and R near the electrode. The asymmetry of the oxidation and reduction current peaks on the CV is largely caused by the diffusion of O and R toward the electrode surface. Such peak-shaped CVs are Faradaic and Nernstian.

S5.3. With the same inactive electrolyte, whilst coating the inert electrode in (**S5.1**) with a thin layer (< 1 μm in thickness) of electronically non-conducting or poorly conducting but reversibly redox active material (e.g. polyvinyl ferrocene), the CV will show a couple of current peaks as presented in **Fig. S5**c. This behaviour is also Faradaic and Nernstian, because there is electron transfer crossing the interface between the electrode and its coating, and both oxidation and reduction currents follow Nernst's Equation.

The main difference between (**S5.2**) and (**S5.3**) is that with increasing the polarisation on the electrode, the current flow on the CV of (**S5.2**) will become controlled by diffusion of O or R in the liquid electrolyte (shown by the high post-peak current at more positive potentials in **Fig. S5**b, resulting from diffusion), but this does not occur in (**S5.3**) if the electrode polarisation remains in the potential range of current peaks as shown by the near-zero post-peak current in **Fig. S5**c. Experimentally, the CV current, particularly the peak current, I_p, is proportional to the square root of the scan rate, v, in (**S5.2**), i.e. $I_p \propto v^{1/2}$ which is in line with the inset of **Fig. S5**b, but it is proportional to the scan rate in (**S5.3**), i.e. $I_p \propto v$.

S5.4. Replacing the non-conducting or poorly conducting coating in (**S5.3**) by an electronically conducting (actually semiconducting in almost all cases) and reversibly redox active material (e.g. polypyrrole or MnO_x), the CV recorded in a proper potential range will be rectangular as shown in **Fig. S5**d. This behaviour is Faradaic and also capacitive, but it does not follow the Nernst Equation. Charge storage in such a coating is truly via the so called pseudocapacitance.

S5.5. When coated as a thin layer on the electrode, many redox active materials behave in a compromised way between (**S5.3**) and (**S5.4**), particularly when the material is in a suitable nano-structure, e.g. nanoparticulates. **Fig. S5**e and **S5**f give two typical examples showing both capacitive and Nernstian features. Causes for such mixed Nernstian and capacitive features can be multiple, but it is possible that such behaviour results from Faradaic processes of both pseudocapacitive and Nernstian origins. Unfortunately, many authors have mistaken CVs like those in **Figs. S5**c**, S5**e1, **S5**f1 and **S5**f2 as being pseudocapacitive, particularly in studies of NiO and $Ni(OH)_2$ based nanomaterials.

S5.6. The above mentioned different voltammetric features of a Faradaic process, i.e. (**S5.2**) to (**S5.5**), can be correlated with the well-known semiconductor band model as illustrated in **Fig. S6**. According to this model, the Nernstian process (left side of **Fig. S6**) will involve the addition or removal of localised valence electrons into or from the singular energy levels which corresponding to E^o in Nernst's Equation, leading to peak-shaped CVs. However, the pseudocapacitive process (middle-right side of **Fig. S6**) corresponds to the transfer of partially delocalised valence electrons over a wide range of energy levels or an energy band. This means that electrons will continue to flow over a wide potential range, forming the capacitive current.

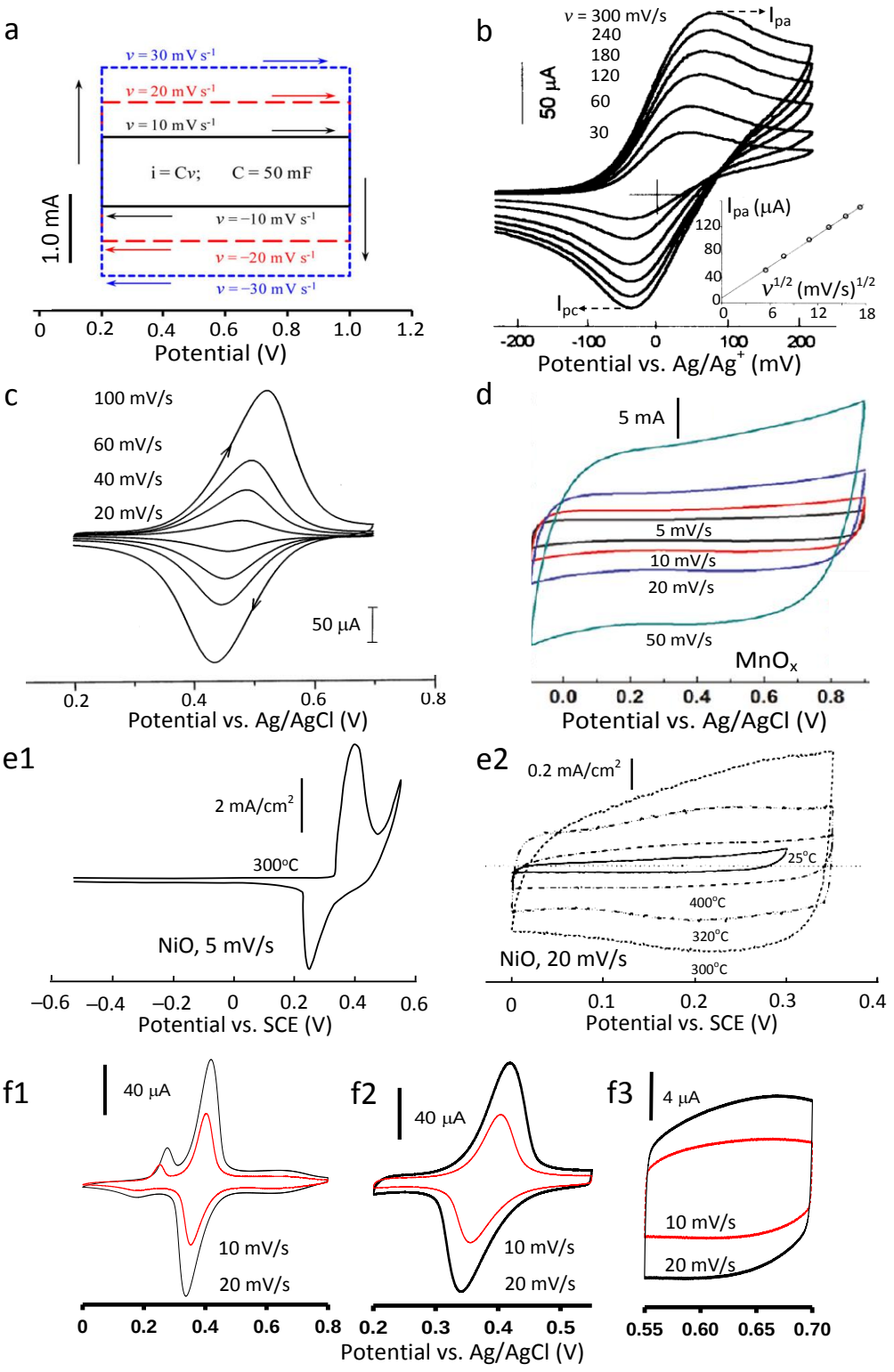

Fig. S5. CVs of different features (cf. Section S5). (**a**) Calculated capacitive CVs of an EDL electrode with C = 50 mF (cf. **S5.1**);[24] (**b**) Nernstian CVs of a ferrocene compound dissolved in organic electrolyte (cf. **S5.2**);[25] (**c**) Nernstian CVs of a ferrocene containing inactive polymer coated electrode in aqueous electrolyte (cf. **S5.3**);[26] (**d**) Capacitive CVs of a MnO_x coated electrode in aqueous electrolyte (cf. **S5.4**);[27] (**e**) CVs of thermally treated NiO coated electrode in aqueous electrolyte, showing (**e1**) Nernstian and (**e2**) capacitive features in different potential ranges (cf. **S5.5**);[28] (**f**) A ferrocene containing active polymer coated electrode in aqueous electrolyte, showing (**f1**, **f2**) Nernstian and (**f3**) capacitive features in different potential ranges (cf. **S5.5**).[29] All CVs are redrawn from the respective references.

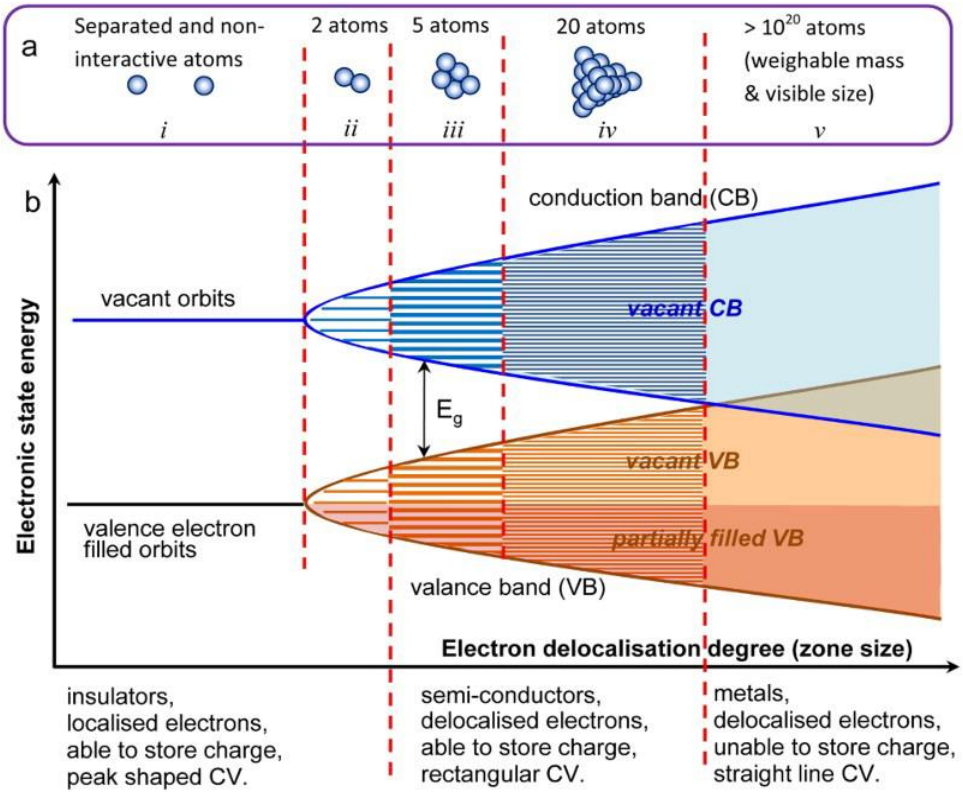

Fig. S6. Schematic illustrations of the band model for chemical bonding [30] (a) between metal atoms that are (i) separated and non-interactive, and (ii – v) forming clusters of (ii) 2, (iii) 5, (iv) 20 and (v) 10^{20} atoms, and (b) the corresponding energy levels of the valence electrons as a function of the degree (or zone size) of delocalisation of valence electrons in the cluster of metal atoms.

S6. Applicability of proposed charge storage mechanism

The author also proposed that the charge storage mechanism discussed in the present work have wider universality and applicability in those pseudocapacitive materials, including the typical transition metal oxides and even the electrical conducting polymers (ECP) who possesses partially delocalised electron states. It has to be emphasised that the electron delocalisation in these materials must be partially confined in whatever dimensional or spatial location elsewhere, such as the delocalised electron states originated from the overlapped d-orbitals of Ru atoms and the p-orbitals of O atoms and segregated by the on-top and bridge site oxygen ions in real spatial lattice of RuO_2.[31] Another very recent publications [32] proposed a series of insertion ions-introduced "charge-switching states" in between the energy gap may be responsible for the pseudocapacitive charge storage in α-MnO_2, although this phase has a wide indirect energy gap about 2.7 eV. Theoretically, if judge the nature of these specific electronic structures, one can immediately find that they are intrinsically partial delocalisation states originated from the restriction of the tunnel structure in MnO_2 crystal lattice. In terms of ECP, the discontinuous conjugated-π bonds again forms its unique delocalisation system, and may contribute on the as-observed pseudocapacitive behaviour. But undoubtedly, more efforts have to be given on these specific materials from both fundamental sight view and more solid bench mark in future work.

References

1 Z. Yang, F. Dang-Qi, Z. Sheng-Li, W. Yu-Hua, Z. Zi-Zhong, *EPL (Europhysics Letters)* 2014, **105**, 37005.

2 U. Hofmann, A. Frenzel and E. Csalán, *Justus Liebigs Annalen der Chemie*, 1934, **510**, 1-41.

3 U. Hofmann and R. Holst, *Berichte der deutschen chemischen Gesellschaft (A and B Series)*, 1939, **72**, 754-771.

4 J. Weiss, *Nature*, 1940, **145**, 719-756.

5 W. Cai, R. D. Piner, F. J. Stadermann, S. Park, M. A. Shaibat, Y. Ishii, D. Yang, A. Velamakanni, S. J. An, M. Stoller, J. An, D. Chen and R. S. Ruoff, *Science*, 2008, **321**, 1815-1817.

6 A. Lerf, H. He, M. Forster and J. Klinowski, *The Journal of Physical Chemistry B*, 1998, **102**, 4477-4482.

7 P. V. Kumar, M. Bernardi and J. C. Grossman, *ACS Nano*, 2013, **7**, 1638-1645.

8 V. Sihvonen, *Transactions of the Faraday Society*, 1938, **34**, 1062-1074.

9 D. Pandey, R. Reifenberger and R. Piner, *Surface Science*, 2008, **602**, 1607-1613.

10 D. Lee, J. Seo, X. Zhu, J. Lee, H.-J. Shin, J. M. Cole, T. Shin, J. Lee, H. Lee and H. Su, *Sci. Rep.*, 2013, **3**.

11 Ž. Šljivančanin, A. S. Milošević, Z. S. Popović and F. R. Vukajlović, *Carbon*, 2013, **54**, 482-488.

12 K. Erickson, R. Erni, Z. Lee, N. Alem, W. Gannett and A. Zettl, *Advanced Materials*, 2010, **22**, 4467-4472.

13 J.-A. Yan and M. Chou, *Physical Review B*, 2010, **82**, 125403.

14 J.-A. Yan, L. Xian and M. Y. Chou, *Physical Review Letters*, 2009, **103**, 086802.

15 S. J. Clark, M. D. Segall, C. J. Pickard, P. J. Hasnip, M. J. Probert, K. Refson and M. C. Payn, *Zeitschrift fuer Kristallographie*, 2005, **220**, 567-570.

16 J. P. Perdew, K. Burke and M. Ernzerhof, *Physical Review Letters*, 1996, **77**, 3865-3868.

17 J. L. Mark, T. Stanko and Š. Željko, *Physica Scripta*, 2014, **2014**, 014019.

18 S.-F. Huang, K. Terakura, T. Ozaki, T. Ikeda, M. Boero, M. Oshima, J.-i. Ozaki and S. Miyata, *Physical Review B*, 2009, **80**, 235410.

19 P. Zhu, B. G. Sumpter and V. Meunier, *The Journal of Physical Chemistry C*, 2013, **117**, 8276-8281.

20 H. J. Monkhorst and J. D. Pack, *Physical Review B*, 1976, **13**, 5188-5192.

21 B. G. Pfrommer, M. Côté, S. G. Louie and M. L. Cohen, *Journal of Computational Physics*, 1997, **131**, 233-240.

22 B. C. Wood, T. Ogitsu, M. Otani and J. Biener, *The Journal of Physical Chemistry C*, 2014, **118**, 4-15.

23 H. Gerischer, R. McIntyre, D. Scherson and W. Storck, *The Journal of Physical Chemistry*, 1987, **91**, 1930-1935.

24 G. Z. Chen, Progress in *Natural Science: Materials International*, 2013, **23**, 245-255.

25 Z. Chen, A. J. Pilgrim and P. D. Beer, *Journal of Electroanalical Chemistry*, 1998, **444**, 209-217.

26 J. X. Wang and M. M. Collionson, *Journal of Electroanalical Chemistry*, 1998, **455**, 127-137.

27 W. Xiao, D. Hu, C. Peng and G. Z. Chen, *ACS Applied Materials & Interfaces,* 2011, **3**, 3120-3129.

28 V. Srinivasan and J. W. Weidner, *Journal of The Electrochemical Society*, 2000, **147**, 880-885.

29 C. Peng, X. H. Zhou, G. Z. Chen, F. Moggia, F. Fages, H. Brisset and J. Roncali, *Chemical Communications*, 2008, 6606-6608.

30 G. Z. Chen, *International Materials Reviews*, 2017, **62**, 173-202.

31 V. Ozoliņš, F. Zhou, M. Asta, *Accounts of Chemical Research*, 2013, **46**, 1084-1093.

32 M.J. Young, A.M. Holder, S.M. George, C.B. Musgrave, *Chemistry of Materials*, 2015, **27**, 1172-1180.